Detector driver systems and photometric estimates for RIMAS

Vicki Toy, Alexander Kutyrev, Eric Lyness, Marius Muench, Frederick Robinson, et al.

Vicki L. Toy, Alexander S. Kutyrev, Eric I. Lyness, Marius Muench, Frederick D. Robinson, Gennadiy N. Lotkin, John I. Capone, Sylvain Veilleux, Samuel H. Moseley, Neil A. Gehrels, Stuart N. Vogel, "Detector driver systems and photometric estimates for RIMAS," Proc. SPIE 9147, Ground-based and Airborne Instrumentation for Astronomy V, 91472W (8 July 2014); doi: 10.1117/12.2054767

SPIE.

Event: SPIE Astronomical Telescopes + Instrumentation, 2014, Montréal, Quebec, Canada

Detector driver systems and photometric estimates for RIMAS

Vicki L. Toy[a], Alexander S. Kutyrev[ab], Eric I. Lyness[b] , Marius Muench[c], F. David Robinson[b], Gennadiy N. Lotkin[b], John I. Capone[a], Sylvain Veilleux[a], Samuel H. Moseley[b], Neil A, Gehrels[b], Stuart N. Vogel[a]

[a]University of Maryland, College Park, Department of Astronomy, College Park, MD, USA 20742; [b]NASA Goddard Space Flight Center, 8800 Greenbelt Rd., Greenbelt, MD, USA 20771; [c]Norwegian University of Science and Technology, Department of Telematics, O.S. Bragstads plass 2a, N-7491 Trondheim, Norway

ABSTRACT

The Rapid infrared IMAger-Spectrometer (RIMAS) is a rapid gamma-ray burst afterglow instrument that will provide photometric and spectroscopic coverage of the Y, J, H, and K bands. RIMAS separates light into two optical arms, YJ and HK, which allows for simultaneous coverage in two photometric bands. RIMAS utilizes two 2048 x 2048 pixel Teledyne HgCdTe (HAWAII-2RG) detectors along with a *Spitzer* Legacy Indium-Antimonide (InSb) guiding detector in spectroscopic mode to position and keep the source on the slit. We describe the software and hardware development for the detector driver and acquisition systems. The HAWAII-2RG detectors simultaneously acquire images using Astronomical Research Cameras, Inc. driver, timing, and processing boards with two C++ wrappers running assembly code. The InSb detector clocking and acquisition system runs on a National Instruments cRIO-9074 with a Labview user interface and clocks written in an easily alterable ASCII file. We report the read noise, linearity, and dynamic range of our guide detector. Finally, we present RIMAS's estimated instrument efficiency in photometric imaging mode (for all three detectors) and expected limiting magnitudes. Our efficiency calculations include atmospheric transmission models, filter models, telescope components, and optics components for each optical arm.

Keywords: detectors, RIMAS, photometry, GRB, infrared, efficiency, H2RG, InSb

1. INTRODUCTION

Gamma-ray bursts (GRBs) are the most violent explosions in the universe. GRBs are seconds long bright flashes of radiation that peak in the gamma-ray band and are often accompanied by long afterglows in the X-ray, optical, and radio. Directed flows of ultrarelativistic matter and their subsequent collision with their environment are believed to be the cause of GRBs and GRB afterglows. GRBs are typically separated into two classes based on the duration of the prompt gamma ray emission: short bursts (<2s) and long bursts (>2s). Observational evidence indicates that the progenitors are gravitational power sources associated with supernova events (long GRBs) or compact binary mergers (short GRBs).[1]

The GRB afterglow flux, at a fixed time from the prompt emission, is nearly independent of its redshift.[2] This relationship combined with GRBs' high brightness and simple power-law afterglow spectra makes GRBs excellent probes of the high-redshift universe and the ideal tool for absorption studies.

The Rapid infrared IMAger-Spectrometer's (RIMAS) primary purpose is to observe high redshift ($z \geq 7$) long GRB afterglows within minutes of detection by the Burst Alert Telescope on the *Swift* Observatory. RIMAS is positioned at the Ritchey-Chrétien (RC) f/6.1 focus on the 4.3 meter Discovery Channel Telescope (DCT). The RC cube arrangement allows for quick (<1 min) switch of instruments. The Gamma-Ray Optical and Near-infrared Detector (GROND) detected optical/near-infrared afterglows for 90% of *Swift* long GRBs with X-ray afterglows when observations started within four hours after the burst, and an overall detection rate of 66% for

Author's e-mail: vtoy@astro.umd.edu

Ground-based and Airborne Instrumentation for Astronomy V, edited by Suzanne K. Ramsay, Ian S. McLean, Hideki Takami, Proc. of SPIE Vol. 9147, 91472W · © 2014 SPIE · CCC code: 0277-786X/14/$18 · doi: 10.1117/12.2054767

any time frame.[3] Therefore, rapid response is of utmost importance for GRBs as there is a short window before the afterglow has dissipated beyond detection.

RIMAS can operate in three modes: photometric imaging, low-resolution spectroscopy (R≈30), and high-resolution spectroscopy (R≈4000). We cover the Y (0.97-1.08 μm), J (1.11-1.33μm), H (1.48-1.78μm), and K (2.00-2.39μm) bands. RIMAS separates light into two optical arms, YJ and HK, which allows for simultaneous coverage in two photometric bands with two science grade Teledyne HgCdTe Astronomy Wide Area Infrared Imager with 2K x 2K, Reference Pixels and Guide Mode (HAWAII-2RG) detectors. The surface surrounding our slits is mirrored and directs light to the slit-imaging optics which image the light on a 256x256, ∼80"x80' field of view *Spitzer* Legacy Indium-Antimonide (InSb) detector[4] used as a guider camera in spectroscopy mode to keep the source on the slit.

2. DETECTOR DRIVER SYSTEMS

2.1 HAWAII-2RG Detector Driver

RIMAS utilizes two HAWAII-2RG detectors simultaneously for multiple wavelength coverage. We are using two sets of identical controllers from Astronomical Research Cameras, Inc (ARC).[5] Each set includes a PCI card (ARC-64), timing board (ARC-22), clock driver (ARC-32), and four video boards (ARC-46). We run the HAWAII-2RG detectors in 100kHz 32-channel mode and acquire images in up-the-ramp sampling mode.

We have three layers of software that control the ARC hardware. The first layer is assembly code written for a Motorola DSP56300 that set the clocks, biases, and acquisition mode. The second layer is the ARC Application Programming Interface (API) written in C++ which allows the user to acquire multiple images from the detector. The first two layers are the standard software for ARC components (although the DSP code is alterable and can be configured for different detectors). The third and last layer of our software is a custom C++ wrapper developed in our laboratory that can run both of our HAWAII-2RG detectors either simultaneously or separately on different PCI cards.

We run the software on a Linux computer that can be accessed remotely and is fully dedicated to driving the detectors to avoid timing delays. The Linux computer will communicate over fiber optic cables to the Labview-based RIMAS control system.

2.2 Slit-viewer InSb Detector Driver

We have developed and built our InSb detector driver system based on National Instruments Compact-RIO (cRIO) controller. Our cRIO-9074 utilizes four modules: a high-speed digital I/O (NI-9401), a custom optoisolator, a digital I/O (NI-9403), and an analog-to-digital converter (NI-9223). The cRIO is controlled by a Labview 11 SP1 GUI and acts as both the detector driver and acquisition system (fig. 1) in conjunction with three external boards: voltage level setter, programmable bias, and amplifier. We have developed a custom set of Labview programs that are alterable and user-friendly.

This system is very versatile, robust, and can be made using commercial off-the-shelf products. The cRIO-9074 has eight module slots which allows us to use two additional modules to monitor temperature diodes and run a passive heater in our testbed system. We acquire images from the InSb detector in 4-channel Fowler[6] sampling mode. The cRIO-9074 is a dedicated detector driver and acquisition system that interfaces with the control computer over ethernet.

The clocking patterns are written in an easily alterable ASCII file that are parsed to our cRIO FPGA and transmitted to an external voltage level-setter board via the NI-9401 and optoisolator. The cRIO also generates commands to an external programmable bias board through the NI-9403. Finally, the NI-9223 converts differential analog signals from the ∼15K InSb detector after they have passed through an external amplifier. While it has been developed for the 256x256 InSb detector, this set of hardware/software can be modified for other systems due to its modifiable clocks and biases. The last remaining problem is reducing periodic pickup noise from the system (see Section 3.1).

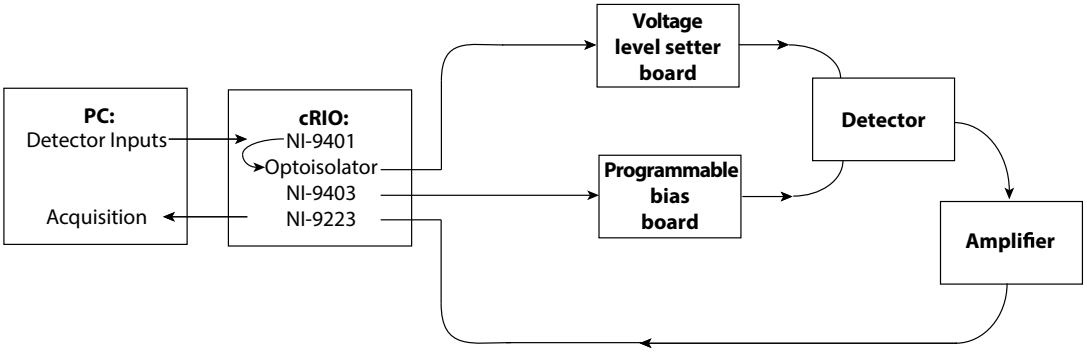

Figure 1. Block diagram of Labview clocking and acquisition system. This is a simple self contained system run primarily by the cRIO with a Labview user interface on a PC connected by ethernet.

3. SLIT-VIEWER DETECTOR CHARACTERIZATION

The InSb detector is used in the slit-viewer system used for guiding while in spectroscopic mode. This detector's primary job is to identify bright objects, therefore, we selected our detector out of our 12 available spare *Spitzer* Legacy InSb arrays based on read noise, linearity, and dynamic range.

3.1 Read Noise

We calculated the conversion gain of our detector by finding the slope of the measured signal vs. the signal's variance. We placed a diffuser on our testbed system and used fluorescent room lights as a uniform source. This created a generally flat-field image. We varied the exposure times to increase the signal and take images for five different Fowlers frames to ensure that the conversion gain is consistent for the different modes. We visually inspected the image and selected a small (50 x 50 pixel) visually uniform area to calculate the mean signal and variance (fig. 2). We removed the pixel-to-pixel variation by using the variance of the difference between two images with the same Fowler number and exposure time. The exposure times (0.1s, 2s, 10s, 20s, 50s, 70s, 100s, 110s, 125s, 150s, 200s) were chosen to sample the dynamic range of the detector from the noise floor to saturation. We performed a linear fit on the data for the first six exposure times for each Fowler mode: these points fell within the linear regime of the detectors based on visual inspection. The inverse of the slope is the conversion gain in e^-/mV (see tab. 1).

Table 1. Electron-voltage conversion and read noise for InSb detector for different Fowler read modes.

Fowler Number	Electron-Voltage Conversion [e^-/mV]	Read Noise [e^-]
1	47.03	36.02
2	46.99	25.93
4	45.77	28.35
8	46.76	28.51
16	48.77	26.84

We then took 10 bias images for the five Fowler modes. We took the difference of pedestal and signal exposure frames and calculated the median from a mean subtracted frame of the 10 images to get the read noise (see table 1). Our testbed system did not have a shutter so the bias frames are not completely dark. This is not noticeable for the smaller Fowler numbers, but starts to have a significant effect by Fowler 4 (fig. 3). This effect was reduced by using a small dark region of the image to calculate the read noise. Note that the read noise does not decrease as a function of $\sqrt{N}$ expected for white noise dominated read noise beyond Fowler 2. This

discrepancy can be attributed to periodic pickup noise and higher Fowler numbers starting to pick up signal due to longer acquisition times.

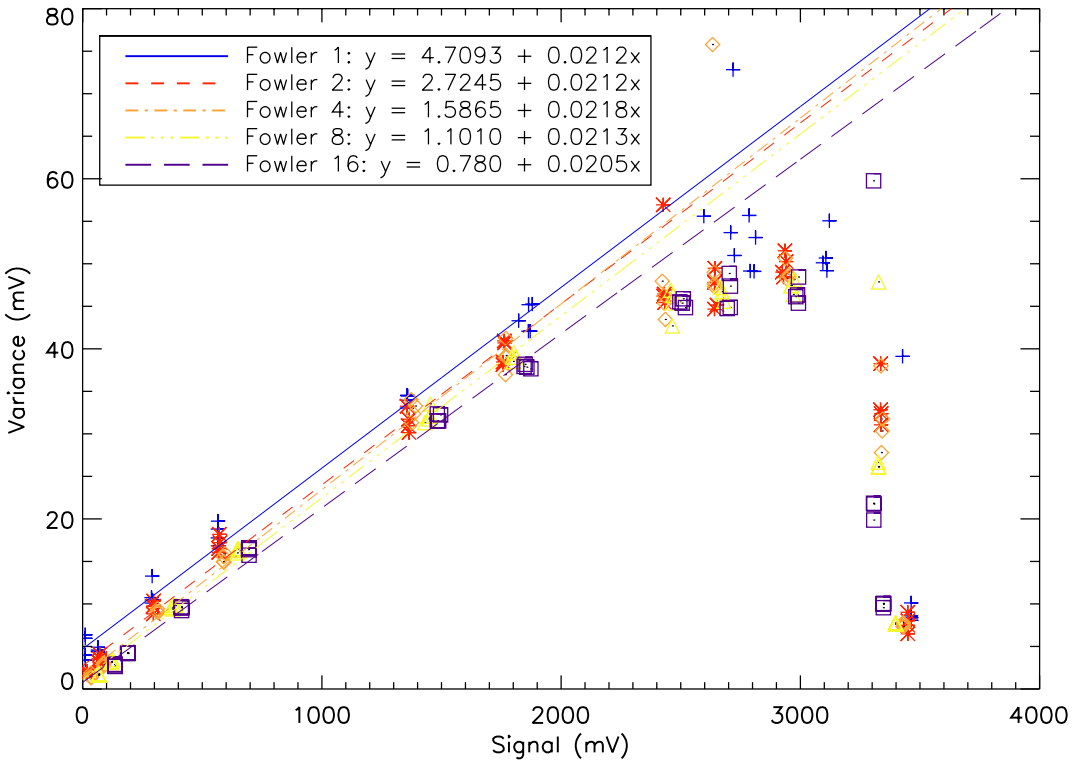

Figure 2. Chosen detector 411448. Non-linear behavior starts at ∼2.7V and completely saturates at ∼3.3V. We calculate the electron-voltage conversion from the slope of the linear region (first 6 exposure times) for each Fowler mode.

Our Fourier signal analysis shows that significant contribution to the noise comes from periodic pickup, thus the read noise can be significantly reduced by shielding and grounding our harnesses carefully. Further work needs to be done to improve the noise of this system before it is used in the actual instrument.

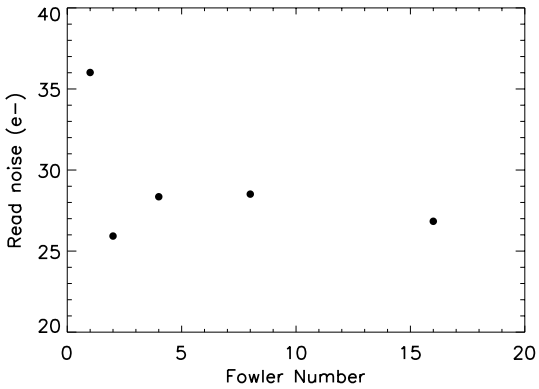

Figure 3. Read noise drops off with larger Fowler frames. Can decrease the read noise by taking more frames with a tradeoff in acquisition speed. Note that for Fowler 4 there is an increase in read noise, this is due to the long acquisition times for higher frames starting to pick up signal. We expect this effect to vanish when the frames are taken using a shutter.

3.2 Linearity

In order to calculate the linearity curves for each individual pixel in the detector array, we ran the detector in Fowler 16 mode with a diffuser and a light bulb held at a constant voltage. This resulted in 32 images that increase in signal with time. We plotted the exposure time against the measured signal for each pixel for the 32 images (see fig. 4).

In order to remove the bias from the non-uniformity of the source and the read circuitry variation between pixels, we forced each pixel to start at 0V. Each pixel has a different gain, so we scaled the array by the slope of the first pixel in the array. The data are tightly bunched for early exposure times but have a wide spread of $\sim$1V at saturation. This is due to the fact that while the pixels appear to be well fit to the first pixel in the linear regime, the pixels strongly deviate in the non-linear regime. This allows us to measure the pixels' deviation from linearity. We created a bad pixel map from the pixels that were 3σ from a fit of the slopes in the linear regime. This map matched well with visual inspection of saturated images. We can use our linearity curves to calibrate any pixel in the array.

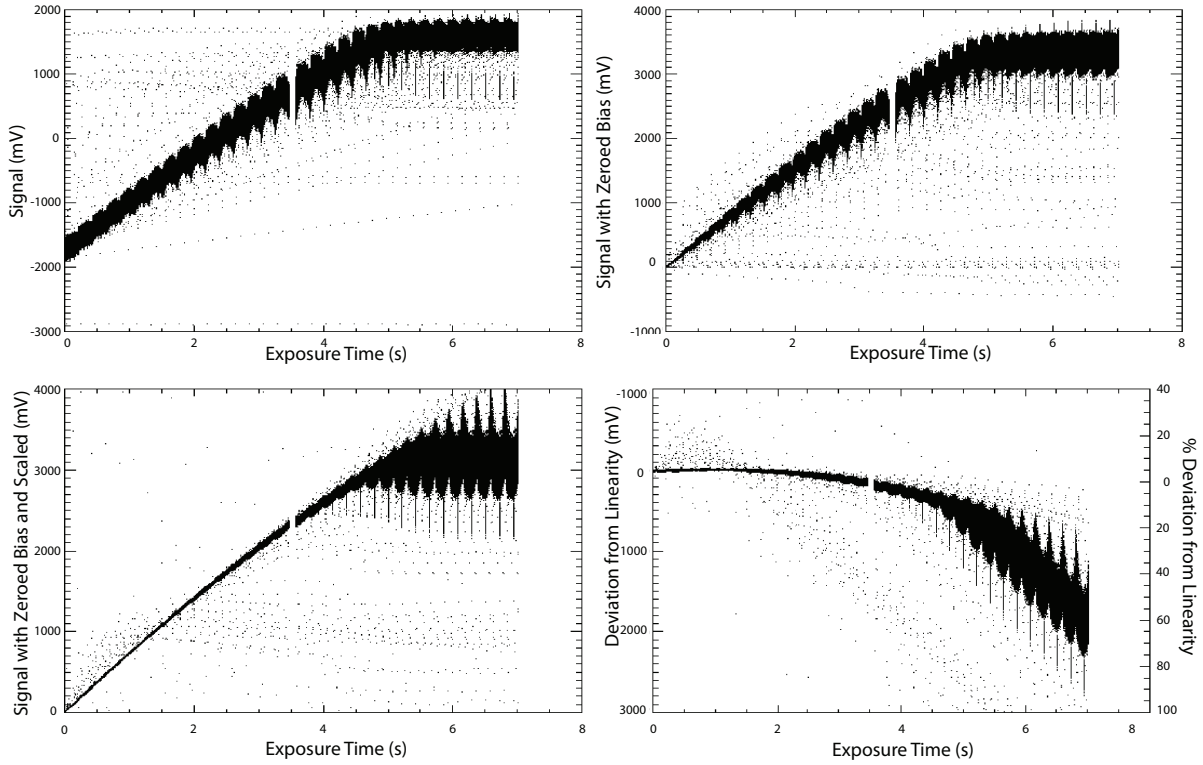

Figure 4. Linearity of detector 411448 from Fowler 16 acquisition. Each black dot represents a pixel for the 32 frames taken, the gap in data at $\sim$3.7s is a 0.1s exposure time for the Fowler. (*upper left*) raw data, (*upper right*) data with the signal offset removed, (*bottom left*) data scaled to the linear fit of the first pixel in the array, (*bottom right*) deviation from linearity in mV and percent. If we ignore the outliers, we can see that there is a large spread in the well depth.

3.3 Dynamic Range

The dynamic range is set at the low end by read noise and the high end by saturation. We defined the upper end of the dynamic range as where the detector deviates 10% from linearity. To find the average dynamic range of the detector we calculated the mean gain, mean saturation, and point where the mean data deviates 10% from linearity (3264mV). Since the read noise for Fowler 16 is 0.55mV, the dynamic range is 37dB. This is a lower limit because our read noise measurement has not been carried out with a shutter.

4. SCIENCE IMPLICATIONS

4.1 InSb Limiting Magnitude

The InSb detector will be used as a guider during both high- and low-resolution spectroscopy mode. The detector will need to quickly relay position corrections to DCT and will guide on either the host galaxy or guide stars.

In Section 3 we characterized the InSb detector and calculated the read noise. We make the assumption that the detector met the *Spitzer* specifications of 1 e^-/s dark current. Since we did not measure the quantum efficiency, we made a conservative estimate of 70% based on previous *Spitzer* testing on similar grade InSb detectors from the same batch. This leads to an overall instrument efficiency of 33%.

Table 2. InSb Detector Limiting Magnitude Estimates SN=10. [a]JH band is taken assuming background limited by H band and that there are no additional losses between bands.

Photometric Band	AB Magnitude or $t_{int} = 1s$	AB Magnitude for $t_{int} = 2s$	AB Magnitude for $t_{int} = 5s$
Y	18.55	19.06	19.65
J	18.58	19.01	19.55
H	17.93	18.32	18.83
JH[a]	18.45	18.83	19.34

Table 3. InSb Detector Limiting Magnitude Estimates SN=5. [a]JH band is taken assuming background limited by H band and that there are no additional losses between bands.

Photometric Band	AB Magnitude or $t_{int} = 1s$	AB Magnitude for $t_{int} = 2s$	AB Magnitude for $t_{int} = 5s$
Y	19.33	19.83	20.42
J	19.35	19.78	20.31
H	18.69	19.08	19.58
JH[a]	19.21	19.59	20.09

Our InSb arrays are sensitive up to ∼5.4μm, however, the atmosphere is not transparent over this entire band. In order to choose a filter for this InSb, we ran calculations of limiting magnitudes for Y, J, H, and JH filters for signal-to-noise ratios of 10 (Table 2) and 5 (Table 3). These are extremely conservative estimates and represent lower limits for the final system. It appears that the best filter choice is a standard broadband J filter.

The host galaxy magnitude drops off quickly with redshift.[7] Even with our highest limiting magnitudes, we will be unable to guide on host galaxies of z≥0.5. Although the GRB afterglow will be observable, almost all of the light from the GRB will be directed into the spectroscopic slit and we will be unable to use the afterglow as a guider other than sending position corrections when the afterglow shifts into view on the InSb detector. This will be more difficult to model. The preferred method is to use a guide star. Thus, we calculated the probability that at least one guide star is in our field of view.

The Two Micron All Sky Survey (2MASS)[8] is a useful tool for finding the number of stars within a field based on magnitude, however, 2MASS is only complete up to ∼15.5-16 J magnitude. We used the Diffuse Infrared Background Experiment (DIRBE) Faint Source Model[9] predictions for the cumulative counts of stars per square degree with our limiting magnitude for three fields (from private communication with Rick Arendt): (l,b)=(5, 20), (l,b)=(75, -75), and (l,b)=(90, 30).

We calculated the probability of finding at least 1 guide star in each of our three test fields for a standard broadband J filter with t_{int}=1s for SN=10 (Table 4) and SN=5 (Table 5). At moderately low galactic latitudes

Table 4. Guide Stars SN=10

Field (l,b)	N(<m=18.58) (stars/deg^2)	λ (stars/FOV)	P(0)	P(n>0)
(5,20)	2.5e4	12.35	4.35e-6	∼1
(75,-75)	2.4e3	0.69	0.50	0.50
(90,30)	7.8e3	2.17	0.11	0.89

Table 5. Guide Stars SN=5

Field (l,b)	N(<m=19.35) (stars/deg^2)	λ (stars/FOV)	P(0)	P(n>0)
(5,20)	5.0e4	12.35	4.35e-6	∼1
(75,-75)	2.6e3	1.28	2.77e-1	0.72
(90,30)	8.4e3	4.15	1.58e-2	0.98

there is a >98% probability of finding a reference star if we relax our signal-to-noise limit. At higher galactic latitudes there is ∼70% probability of finding a guide star. In order to have a 99% probability of finding a guide star at these latitudes, our limiting magnitude would have to be ≥24.9 AB which is not realistic for the short integration times required for a guiding camera. Thus, there will be a high probability of guide stars in moderately low galactic latitudes and if there are no guide stars in the high galactic latitudes we will have to guide on the afterglow source that shifts off the spectroscopic slit.

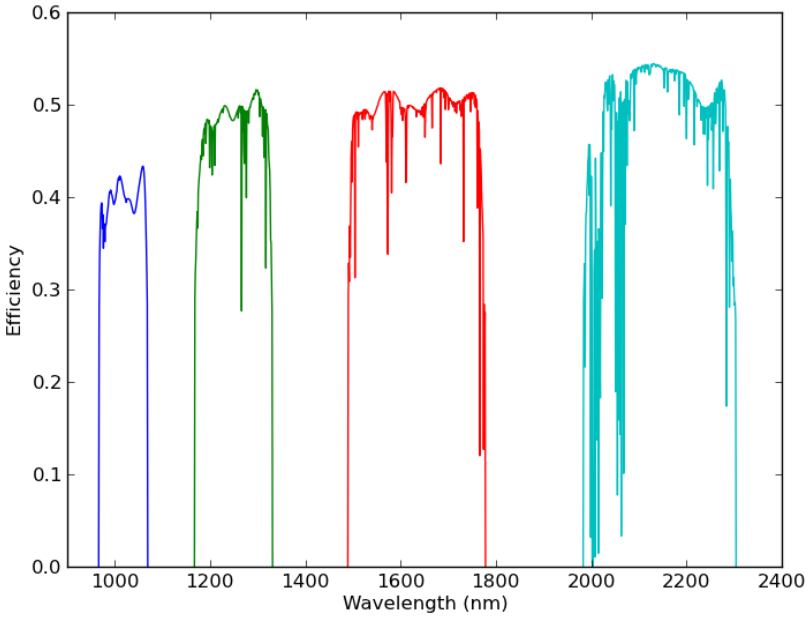

Figure 5. Total estimated efficiency of science detectors in photometric imaging mode.

4.2 HAWAII-2RG Limiting Magnitude

Although we have not characterized the HAWAII-2RGs yet, we can make an estimate on the limiting magnitude based on measurements of similar detectors. We assumed that the dark current is 0.005 e^-/s, the read noise is 6 e^-, and the quantum efficiency is 70%, these are conservative estimates. Combined with our mirror data, lens models, window models, and atmospheric transmission models, this results in a ∼40-55% instrument efficiency in photometric imaging mode (see fig. 5 for photometric band efficiencies). Since the afterglow light curve follows a power law and we are interested in viewing each photometric band, it is likely that our observations will be on the order of 100s of seconds.

Table 6 shows how RIMAS compares to existing similar ground-based near-infrared photometric imaging GRB follow-up instruments. We used our instrument efficiency model to do a direct comparison of RIMAS to the Reionization And Transients InfraRed camera (RATIR),[10] GROND,[11] Peters Automated Infrared Imaging Telescope (PAIRITEL),[12] and Gemini's Near InfraRed Imager and Spectrometer (NIRI).[13] The last column shows how deep RIMAS would see in AB magnitudes with the same filter, exposure time, and signal-to-noise that these instruments report their limiting magnitudes with.

Table 6. Photometric imaging instrument limiting magnitude comparison chart. [a]Converted to AB magnitude using Ref. 14 except L', M'.

Instrument	Telescope size	Filters	AB mag	Exposure Time	S/N	RIMAS exact comparison
RATIR	1.5m	r	22.5	960 sec	10	-
		i	22.3	960 sec	10	-
		Z	21.2	960 sec	10	-
		Y	20.8	960 sec	10	22.69
		J	20.9	960 sec	10	22.67
		H	20.1	960 sec	10	21.89
GROND	2.2m	g	24.2	480 sec	3	-
		r	24.2	480 sec	3	-
		i	23.7	480 sec	3	-
		z	23.5	480 sec	3	-
		J	21.4	480 sec	3	23.61
		H	20.4	480 sec	3	22.82
		K	19	480 sec	3	22.34
PAIRITEL	1.3m	J	∼18	1800 sec	5	23.77
		H	∼17.5	1800 sec	5	22.99
		Ks	∼17	1800 sec	5	22.5
NIRI[a]	8.1m	J	24.41	3600 sec	5	24.15
		H	23.84	3600 sec	5	23.36
		K	24.46	3600 sec	5	22.88
		L'	17 mag	3600 sec	5	-
		M'	14.4 mag	3600 sec	5	-

5. SUMMARY

RIMAS's detector driver hardware and software have been finalized. We use two types of commercial-off-the-shelf hardware systems (ARC and NI cRIO) for the clocking and acquisition of our detectors. We have developed

and tested custom software programs for the InSb driver that are versatile and easily programmable. The RIMAS InSb slit-viewer detector has been characterized with this new robust detector driver system. We have reported read noise, linearity, and dynamic range measurements for the InSb detector. These can and will be improved with better harness shielding and software to remove periodic noise. Both HAWAII-2RG detectors will be characterized in the near future using the ARC hardware and our C++ wrapper software to run both detectors simultaneously. We report imaging limiting magnitude estimates for all three of our detectors and direct comparison with similar instruments. In winter of 2014, RIMAS will be commissioned.

ACKNOWLEDGMENTS

We would like to thank NASA Goddard's Detector Characterization Laboratory (DCL) for their time, expertise, and advice in running the HAWAII-2RG detectors, in particular Augustyn Waczynski and Peter Kenny. We also thank Chris Bebek for loaning RIMAS one of the SNAP HAWAII-2RG detectors. VLT thanks the NASA Earth and Space Science Fellowship (NESSF) for financial support.

REFERENCES

[1] Gehrels, N., Ramirez-Ruiz, E., and Fox, D., "Gamma-Ray Bursts in the Swift Era," ARA&A **47**, 567–617 (2009).

[2] Ciardi, B. and Loeb, A., "Expected Number and Flux Distribution of Gamma-Ray Burst Afterglows with High Redshifts," ApJ **540**, 687–696 (2000).

[3] Greiner, J., Krühler, T., Klose, S., Afonso, P., Clemens, C., Filgas, R., Hartmann, D. H., Küpcü Yoldaş, A., Nardini, M., Olivares E., F., Rau, A., Rossi, A., Schady, P., and Updike, A., "The nature of "dark" gamma-ray bursts," A&A **526**, A30 (2011).

[4] Fazio, G. G., Hora, J. L., Allen, L. E., Ashby, M. L. N., Barmby, P., Deutsch, L. K., Huang, J.-S., Kleiner, S., Marengo, M., Megeath, S. T., Melnick, G. J., Pahre, M. A., Patten, B. M., Polizotti, J., Smith, H. A., Taylor, R. S., Wang, Z., Willner, S. P., Hoffmann, W. F., Pipher, J. L., Forrest, W. J., McMurty, C. W., McCreight, C. R., McKelvey, M. E., McMurray, R. E., Koch, D. G., Moseley, S. H., Arendt, R. G., Mentzell, J. E., Marx, C. T., Losch, P., Mayman, P., Eichhorn, W., Krebs, D., Jhabvala, M., Gezari, D. Y., Fixsen, D. J., Flores, J., Shakoorzadeh, K., Jungo, R., Hakun, C., Workman, L., Karpati, G., Kichak, R., Whitley, R., Mann, S., Tollestrup, E. V., Eisenhardt, P., Stern, D., Gorjian, V., Bhattacharya, B., Carey, S., Nelson, B. O., Glaccum, W. J., Lacy, M., Lowrance, P. J., Laine, S., Reach, W. T., Stauffer, J. A., Surace, J. A., Wilson, G., Wright, E. L., Hoffman, A., Domingo, G., and Cohen, M., "The Infrared Array Camera (IRAC) for the Spitzer Space Telescope," ApJS **154**, 10–17 (2004).

[5] Leach, R. W. and Low, F. J., "CCD and IR array controllers," in [*Optical and IR Telescope Instrumentation and Detectors*], Iye, M. and Moorwood, A. F., eds., *Society of Photo-Optical Instrumentation Engineers (SPIE) Conference Series* **4008**, 337–343 (2000).

[6] Fowler, A. M. and Gatley, I., "Demonstration of an algorithm for read-noise reduction in infrared arrays," ApJ **353**, L33 (1990).

[7] Jakobsson, P., Malesani, D., Hjorth, J., Fynbo, J. P. U., and Milvang-Jensen, B., "GRB host galaxies: An unbiased sample," *Advances in Space Research* **47**, 1416–1420 (2011).

[8] Skrutskie, M. F., Cutri, R. M., Stiening, R., Weinberg, M. D., Schneider, S., Carpenter, J. M., Beichman, C., Capps, R., Chester, T., Elias, J., Huchra, J., Liebert, J., Lonsdale, C., Monet, D. G., Price, S., Seitzer, P., Jarrett, T., Kirkpatrick, J. D., Gizis, J. E., Howard, E., Evans, T., Fowler, J., Fullmer, L., Hurt, R., Light, R., Kopan, E. L., Marsh, K. A., McCallon, H. L., Tam, R., Van Dyk, S., and Wheelock, S., "The Two Micron All Sky Survey (2MASS)," AJ **131**, 1163–1183 (2006).

[9] Arendt, R. G., Odegard, N., Weiland, J. L., Sodroski, T. J., Hauser, M. G., Dwek, E., Kelsall, T., Moseley, S. H., Silverberg, R. F., Leisawitz, D., Mitchell, K., Reach, W. T., and Wright, E. L., "The COBE Diffuse Infrared Background Experiment Search for the Cosmic Infrared Background. III. Separation of Galactic Emission from the Infrared Sky Brightness," ApJ **508**, 74–105 (1998).

[10] Butler, N., Klein, C., Fox, O., Lotkin, G., Bloom, J., Prochaska, J. X., Ramirez-Ruiz, E., de Diego, J. A., Georgiev, L., González, J., Lee, W. H., Richer, M. G., Román, C., Watson, A. M., Gehrels, N., Kutyrev, A., Bernstein, R., Alvarez, L. C., Ceseña, U., Clark, D., Colorado, E., Córdova, A., Farah, A., García, B., Guisa, G., Herrera, J., Lazo, F., López, E., Luna, E., Martínez, B., Murillo, F., Murillo, J. M., Núñez, J. M., Pedrayes, M. H., Quirós, F., Ochoa, J. L., Sierra, G., Moseley, H., Rapchun, D., Robinson, F. D., Samuel, M. V., and Sparr, L. M., "First Light with RATIR: An Automated 6-band Optical/NIR Imaging Camera," in [*Society of Photo-Optical Instrumentation Engineers (SPIE) Conference Series*], *Society of Photo-Optical Instrumentation Engineers (SPIE) Conference Series* **8446** (2012).

[11] Greiner, J., Bornemann, W., Clemens, C., Deuter, M., Hasinger, G., Honsberg, M., Huber, H., Huber, S., Krauss, M., Krühler, T., Küpcü Yoldaş, A., Mayer-Hasselwander, H., Mican, B., Primak, N., Schrey, F., Steiner, I., Szokoly, G., Thöne, C. C., Yoldaş, A., Klose, S., Laux, U., and Winkler, J., "GROND - a 7-Channel Imager," PASP **120**, 405–424 (2008).

[12] Bloom, J. S., Starr, D. L., Blake, C. H., Skrutskie, M. F., and Falco, E. E., "Autonomous Observing and Control Systems for PAIRITEL, a 1.3m Infrared Imaging Telescope," in [*Astronomical Data Analysis Software and Systems XV*], Gabriel, C., Arviset, C., Ponz, D., and Enrique, S., eds., *Astronomical Society of the Pacific Conference Series* **351**, 751 (2006).

[13] Hodapp, K. W., Jensen, J. B., Irwin, E. M., Yamada, H., Chung, R., Fletcher, K., Robertson, L., Hora, J. L., Simons, D. A., Mays, W., Nolan, R., Bec, M., Merrill, M., and Fowler, A. M., "The Gemini Near-Infrared Imager (NIRI)," PASP **115**, 1388–1406 (2003).

[14] Campins, H., Rieke, G. H., and Lebofsky, M. J., "Absolute calibration of photometry at 1 through 5 microns," AJ **90**, 896–899 (1985).